

Effect of measurement reduction on synthetic aperture x-ray ghost imaging

Haipeng Zhang(张海鹏), Jie Tang(汤杰), Nixi Zhao(赵尼西), Changzhe Zhao(赵昌哲), Jianwen Wu(吴建文), Zhongliang Li(李中亮), and Tiqiao Xiao(肖体乔)

Citation: Chin. Phys. B, 2026, 35 (**1**): 014204. DOI: 10.1088/1674-1056/ae07ab
http://cpb.iphy.ac.cn; http://iopscience.iop.org/cpb

What follows is a list of articles you may be interested in

Entropy evolution law of a general linear state for diffusion noise

Yingyu Zhang(张映玉) and Yixing Wang(王依兴)
Chin. Phys. B, 2025, 34 (**9**): 094206. DOI: 10.1088/1674-1056/add4f2

Single exposure passive three-dimensional information reconstruction based on an ordinary imaging system

Shen-Cheng Dou(窦申成), Fan Liu(刘璠), Hu Li(李虎), Xu-Ri Yao(姚旭日), Xue-Feng Liu(刘雪峰), and Guang-Jie Zhai(翟光杰)
Chin. Phys. B, 2023, 32 (**11**): 114204. DOI: 10.1088/1674-1056/ace764

Efficient implementation of x-ray ghost imaging based on a modified compressive sensing algorithm

Haipeng Zhang(张海鹏), Ke Li(李可), Changzhe Zhao(赵昌哲), Jie Tang(汤杰), and Tiqiao Xiao(肖体乔)
Chin. Phys. B, 2022, 31 (**6**): 064202. DOI: 10.1088/1674-1056/ac48f7

An image compressed sensing algorithm based on adaptive nonlinear network

Yuan Guo(郭媛), Wei Chen(陈炜), Shi-Wei Jing(敬世伟)
Chin. Phys. B, 2020, 29 (**5**): 054203. DOI: 10.1088/1674-1056/ab7b4e

Compressed ghost imaging based on differential speckle patterns

Le Wang(王乐), Shengmei Zhao(赵生妹)
Chin. Phys. B, 2020, 29 (**2**): 024204. DOI: 10.1088/1674-1056/ab671a

---

Effect of measurement reduction on synthetic aperture x-ray ghost imaging

Haipeng Zhang(张海鹏)[1], Jie Tang(汤杰)[1,2,3], Nixi Zhao(赵尼西)[1,2,3], Changzhe Zhao(赵昌哲)[4], Jianwen Wu(吴建文)[1,2,3], Zhongliang Li(李中亮)[1], and Tiqiao Xiao(肖体乔)[1,2,3,†]

[1] *Shanghai Synchrotron Radiation Facility, Shanghai Advanced Research Institute, Chinese Academy of Sciences, Shanghai* 201204, *China*
[2] *Shanghai Institute of Applied Physics, Chinese Academy of Sciences, Shanghai* 201800, *China*
[3] *University of Chinese Academy of Sciences, Beijing* 100049, *China*
[4] *Shanghai Institute of Microsystems and Information Technology, Chinese Academy of Sciences, Shanghai* 200233, *China*

(Received 10 April 2025; revised manuscript received 10 June 2025; accepted manuscript online 17 September 2025)

The unique advantage of x-ray ghost imaging (XGI) is its potential in low dose radiology. One of the practical ways to reduce the radiation exposure is to reduce the measurements while remaining sufficient image quality. Synthetic aperture x-ray ghost imaging (SAXGI) is invented to achieve megapixel XGI with limited measurements, which is expected to implement XGI simultaneously with large field of view and low radiation exposure. In this paper, we experimentally investigate the effect of measurements reduction on the spatial resolution and image quality of SAXGI with standard sample and biomedical specimen. The results with a resolution chart demonstrated that at 360 measurements, SAXGI successfully retrieved the sample image of 1960×1960 pixels with spatial resolution of 4 μm. With measurement reduction, the spatial resolution deteriorates but the sparser structures are still discernable. Even with measurements reduced to 10, a spatial resolution of 10 μm can still be achieved by SAXGI. A biomedical sample of a fish specimen is employed to evaluate the method and the fish image of 2000×1000 pixels with an SSIM of 0.962 is reconstructed by SAXGI with 770 measurements, corresponding to an accumulative exposure reduction of more than 2 times. With the measurements reduced to 10 which corresponds to 1/160 of the accumulative radiation exposure for conventional radiology, bulky structure like the fish skeleton can still be definitely discerned and the SSIM for the reconstructed image still retained 0.9179. Results of this paper demonstrate that measurements reduction is practicable for the radiation exposure reduction of the sample, which implicates that SAXGI with limited measurements is an efficient solution for low dose radiology.

Keywords: x-ray ghost imaging, synthetic aperture x-ray imaging, low dose radiology, compressed sensing algorithm

PACS: 42.50.–p, 87.59.–e, 42.62.Be, 42.30.–d

DOI: 10.1088/1674-1056/ae07ab **CSTR:** 32038.14.CPB.ae07ab

1. Introduction

The x-ray radiography is an invaluable tool for the analysis of the biological specimens and the detection of nanomaterials. It is widely used for visualizing the morphology of opaque materials, and for assessing quantitative analysis of their geometries and properties.[1–6] However, the mainstream x-ray imaging techniques have faced severe problems such as the inherent tradeoff between the large field-of-view and high resolution, high-flux illumination sources improving the image contrast but also introducing radiation damage to the vulnerable biological organisms.[7] What is more, the resolution of conventional x-ray modalities is also restricted by the source size, the precision of optical components, the pixel resolution of the detector and the thickness of the scintillator converting x-rays into visible light.[8] Therefore, there is an urgent demand for exploring a new x-ray imaging method without sophisticated x-ray optics and high-resolution cameras to lower the requirements for low-dose x-ray microscopy. Fortunately, lensless ghost imaging,[9–12] equipped with high-sensitivity single-pixel detector, combined with high-energy deep-penetration x-rays, has great potential in terms of resolution improvement and dose reduction.

In principle, lensless ghost imaging can be applied to any wavelength, which has been demonstrated experimentally with electrons,[13] atoms,[14] neutrons[15] in addition to x-rays.[7,8,16–33] Owing to its unique advantages, XGI has flourished into diverse domains, such as absorption spectroscopy, fluorescence, computed tomography (CT), scattering, and so on.[19,24,27,34–36] Because of the high sensitivity of the bucket detector in the signal beam, many scholars believe that XGI has a great potential in reducing radiation exposure. Except for the high sensitivity caused by bucket detectors, the high compression ratios introduced by various methods, such as advanced reconstruction algorithms (*e.g.*, deep learning, compressed sensing), mask design and reordering, can also significantly reduce radiation exposure while maintaining adequate image quality.[7,8,21,37–40] All the above works has contributed to the applications of XGI in radiology in terms of radiation

†Corresponding author. E-mail: tqxiao@sari.ac.cn

© 2026 Chinese Physical Society and IOP Publishing Ltd. All rights, including for text and data mining, AI training, and similar technologies, are reserved.

exposure and resolution.

It is well known that the imaging signal-to-noise ratio (SNR) of XGI is closely associated with the pixel number of the reconstructed image, the measurement number, the modulation depth of the mask, and the correlation between the signal and reference beams. However, it is difficult to generate two beams with speckle patterns of identical intensity distribution due to the lack of stable and reliable optical components in x-ray regime, which severely hampers the imaging efficiency and image quality of XGI. To address this issue, a stress-free Laue thin crystal was invented to improve the correlation between the two beams to above 0.9 which helps obtain high-fidelity reconstruction with fewer measurements.[17,33,41] Additionally, various masks were tried to enhance the property of the speckle pattern, *e.g.*, to improve the modulation depth to increase the image contrast and to reduce the feature size of the speckles to enhance the image resolution.[8] Improving the modulation depth not only helps optimize the image contrast but also reduces the requirements for more measurements when maintaining the image fidelity. Some other measures were taken, such as adjusting the order of the masks,[39,42,43] exploring advanced algorithms including compressed sensing[30,44] or deep learning,[38,45,46] to further reduce the measurement number required by high-fidelity imaging. Much fewer measurements not only means faster data acquisition and shorter reconstruction time, but also lower radiation exposure which is of great significance to biomedicine.

Aiming at mega pixels x-ray ghost imaging with limited measurements, synthetic aperture x-ray ghost imaging (SAXGI) is proposed and demonstrated by simulation[29] and experiments,[45] which uses very few measurements to realize high-fidelity reconstruction of the tungsten wire and shows great potential in low dose radiology. However, less measurements may lead to image quality deterioration. In this paper, we investigate systematically the effect of measurements on the image reconstruction of SAXGI, which is critical for low-dose radiology. Firstly the experimental setup, reconstruction algorithm (referred to Ref. [29]) and the property of speckle patterns are introduced. A standard sample and a biomedical specimen are selected to evaluate the image quality of SAXGI. Spatial resolution, peak signal-to-noise ratio (PSNR) and structural similarity (SSIM) index are used to analyze the image quality. Then, the experimental results and analysis are presented. Finally, the conclusions and discussions of this work are given.

2. Experiments

2.1. Experimental setup

The SAXGI experiments were carried out at beamlines of BL09B and BL13HB at Shanghai Synchrotron Radiation Facility (SSRF) with very stable beam current. The x-ray pulses from SSRF can reach picosecond durations. The details of the experimental setup is shown in Fig. 1 and can also be referred to Ref. [29]. The pseudo-thermal x-ray source was produced

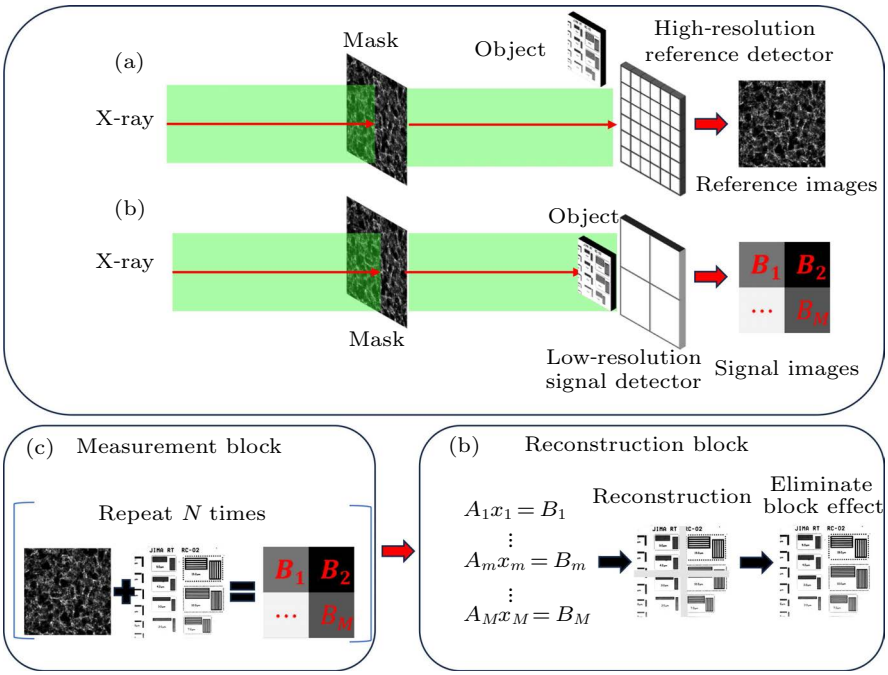


Fig. 1. Scheme of experimental setup for synthetic aperture x-ray ghost imaging (SAXGI). (a) The reference arm where the mask is recorded by the high-resolution reference and (b) the object arm where the signal image is registered by the low-resolution signal detector. (c) The measurement process repeats N times, where $B_m(m = 1, 2, \cdots M) \in R^{N\times 1}$is an observation vector whose elements are the intensity of the jth pixel on the low-resolution signal detector. (d) The compressed sensing algorithm is used to reconstruct the image block. The complete high-resolution image is synthesized from a series of the image block. Some methods, such as globally optimized registration, image filtering algorithms, are utilized to eliminate the block effect to improve the reconstruction quality.

by a raster scan of the sandpaper, illuminated by a monochromatic x-ray beam at the photon energy of 15 keV. This photon energy was chosen because of the high photon flux of the beamline and the high quantum efficiency of the detector in this spectral regime. The sample was mounted 30-cm downstream of the sandpaper, followed by a high-resolution detector placed approximately 0.5 cm from the sample. The high-resolution detector is consisted of a 100-μm-thick scintillator (LuAG:Ce), an optical microscope (model: Optique Peter MICRX016), and a CMOS detector (Hamamatsu ORCA-Flash 4.0 C11440). The basic pixel size of the detector is 6.5 μm while the effective pixel size is equal to the basic pixel size divided by the magnification of the microscope. The magnification of the microscope is usually selected at 2×, 4×, 10×, and 20×, depending on the requirements of exposure time and subtle structure. With the sample out of the x-ray beam, the high-resolution detector is seen as the reference detector recording the random speckle patterns, as shown in Fig. 1(a). With the sample moved into the x-ray beam, a low-resolution signal detector collects the signals modulated by both the sandpaper and the sample, as shown in Fig. 1(b). A shutter is placed upstream of the sample to reduce the radiation damage to the sample. The shutter is triggered by the low-resolution signal detector to open when the signal detector is acquiring the signal images. The pixel of the low-resolution object detector is synthesized through binning over the adjacent pixel of the reference detector. In the following experiments, the low-resolution pixel was artificially synthesized by binning 40×40 pixels on the high-resolution reference detector. This process is repeated N times with the different regions of the sandpaper illuminated by the beam, shown in Fig. 1(c). At last, the 'ghost' image is reconstructed by correlating the signals captured by the low-resolution signal detector with the transmitted illumination patterns registered by the high-resolution reference detector.

2.2. Reconstruction algorithm

In order to overcome the critical issue that XGI needs many measurements to achieve high-quality reconstruction, a block-by-block reconstruction strategy is implemented in both the experimental design and reconstruction algorithms, as shown in Figs. 1(c) and 1(d). Through N measurements, the structural information x_m of the sample within the block area B_m can be reconstructed using the total variation augmented lagrangian alternating direction algorithm (TVAL3)[46] which takes the image smoothness into account and has good noise immunity. For the reconstruction of the block B_m, A_m is the measurement matrix whose k-th row is rearranged from the matrix corresponding to the area of the block B_m in the k-th reference image. B_m is a column vector whose k-th element is from the bucket signal corresponding to the position of the block B_m in the k-th signal image. In other words, the local structural information of the sample is reconstructed from each pixel of the low-resolution signal detector, and then the complete high-resolution image is synthesized from an array of image blocks. The reconstruction parameters of each block are set to be consistent to simplify the algorithm complexity. Finally, the image quality is improved by eliminating the discontinuous blocks in the complete image through globally optimized registration, image filtering algorithms.

2.3. Speckle patterns

Taken by the reference detector shown in Fig. 2(a), the average size of the irregular alumina particles on the sandpaper acted as the mask is about 75 μm according to the mesh of the sandpaper. Through x-ray radiography of the sandpaper and data analysis, the full width at half-maximum (FWHM) of the second-order autocorrelation function of the sandpaper is about 39 μm, close to the average particle radius from both horizontal and vertical perspectives, shown in Fig. 2(d). Actually, the central distribution of the Glauber function is not a standard circle, which means that the spatial resolution is anisotropic in different directions as shown in Fig. 2(c). Moreover, the peak of the function was up to 1.27, theoretically suggesting that the modulation depth meets the requirements of high-quality XGI using very few measurements. The peak position of the probability density function for the speckle grayscale is off the Y-axis, which does not agree with the theoretical negative exponential distribution, shown in Fig. 2(b). Moreover, the peak of the Glauber function is much lower than the theoretical maximum of 2. These indicates that the modulation depth of the experimental sandpaper does not reach the desired effect, and needed to be improved in the future.

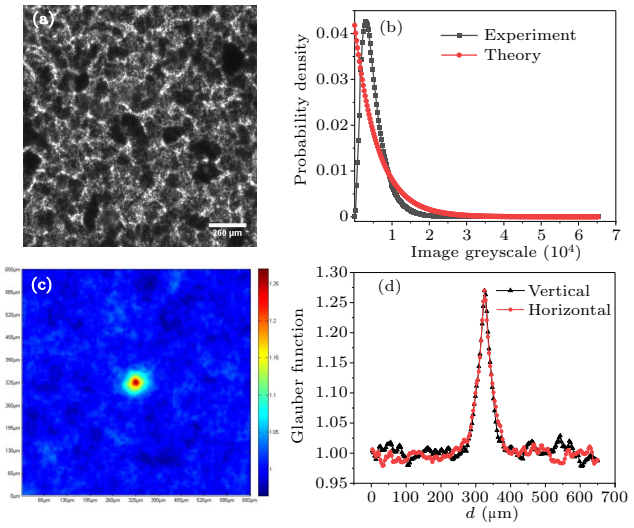


Fig. 2. Experimental sandpaper, where (a) the sandpaper image taken by the detector at the photon energy of 15 keV and the pixel size of 3.25 μm, (b) the probability density distribution of the greyscale for the sandpaper pattern, (c) autocorrelation function over all the speckle patterns, which has the maximum value of 1.27, (d) central line-profile of the autocorrelation function in the horizontal and vertical directions, whose FWHMs were both 39 μm in both horizontal and vertical directions.

3. Experimental results and analysis

3.1. Resolution chart

A resolution chart (RC), a typical binary object with low contrast and relatively simple structure, is utilized to verify the resolution that the SAXGI scheme can achieve at very few measurements. The projection image of RC was shown in Fig. 3(a) with pixel size of 0.65 μm and 1960 × 1960 pixels at an exposure time of 4 s. According to Fig. 3(a), the visibility of RC is about 8.5% at 15 keV due to the grayscale difference between the dark and bright stripes. The lower visibility of the object means more measurements required for SAXGI. Figure 3(b) shows signals of RC recorded by the signal detector with an effective pixel size of 26 μm. The exposure time for each frame in both reference and signal beam is 8 s because 4-layers sandpaper absorbs almost 50% of the x-rays at 15 keV. As the pixel size of the signal detector is much larger than the maximum spacing between stripes in RC, it is evident that the stripe structure is not distinguished by the object detector. Taking the image reconstructed by traditional x-ray ghost imaging (TXGI) as a comparison, there is no doubt that the image shown in Fig. 3(c) provides no valid information about the sample due to ultra-low measurements (only 360 measurements). However, 360 measurements are sufficient for SAXGI to reconstruct high-fidelity 'ghost' images due to the block-to-block strategy. As shown in Fig. 3(d), the RC is successfully retrieved by SAXGI. For RC with a period of 10 μm, the corresponding line profile along with that of the target image is given in Fig. 3(e), which indicates that the positions of peaks and valleys as well as the height of the peaks, the depth of the valleys are consistent with those in the target image. This means that at spatial resolution of 10 μm, the resolution chart can be accurately reconstructed.

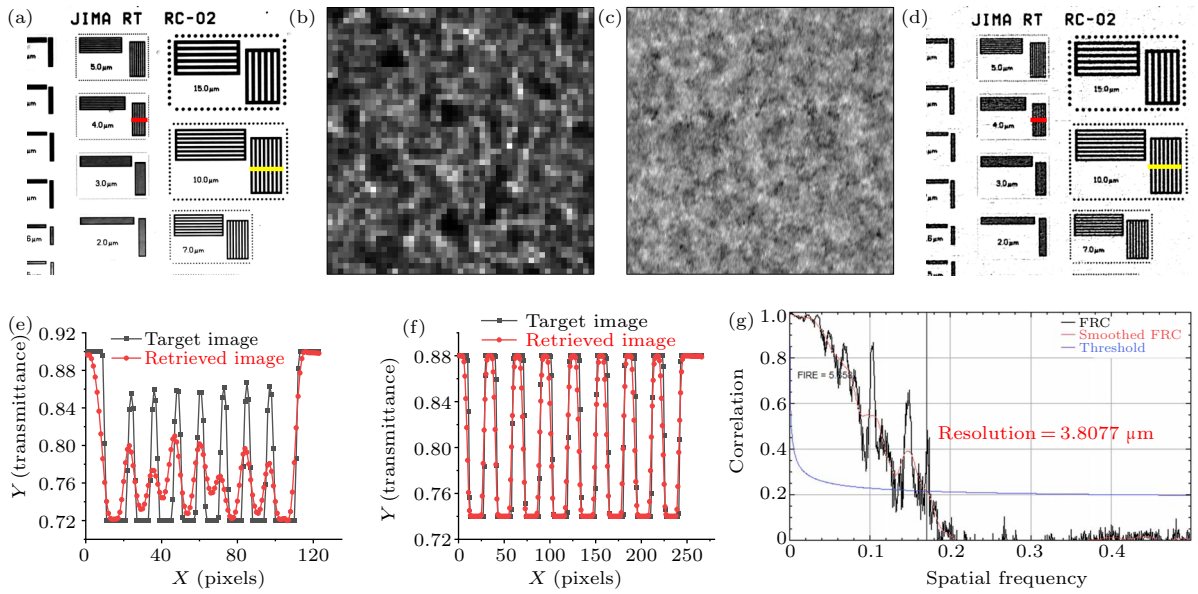


Fig. 3. Experiments with a resolution chart, where (a) the target image obtained by high-resolution reference detector, (b) signals in object beam, (c) the image reconstructed by TXGI, (d) the image reconstructed by SAXGI, (e) line profiles of stripes at spatial resolution of 10 μm as marked with yellow lines in panels (a) and (d), (f) line profiles at spatial resolution of 4 μm as noted with red lines in panels (a) and (d), (g) image resolution analyzed through Fourier ring correlation (FRC) which indicates the resolution of 3.81 μm.

Based on the direct observation to the retrieved image with SAXGI shown in Fig. 3(d), the resolution target at the resolution of 4 μm is distinguishable. The corresponding profiles shown in Fig. 3(f) demonstrate that the positions of the peaks and valleys of the stripes are reconstructed correctly though their heights or depths are smaller than that of the target image, which may be due to insufficient measurements. Moreover, the scattering of the thick scintillator results in the decrease in the imaging resolution and introduced blurring in the detected image. Therefore, the practical imaging resolution would be slightly lower than the pixel resolution. Generally, the imaging resolution was 3 to 5 times the pixel size, which shows that SAXGI is close to the limit of the detector. Anyway, it is reasonable to conclude a spatial resolution of 4 μm was achieved in this experiment at only 360 measurements. Moreover, we come to the same conclusion that the spatial resolution can reach 3.81 μm by the analysis of Fourier ring correlation (FRC), as shown in Fig. 3(g). In principle, higher sampling rate will result in higher fidelity and higher spatial resolution of the restored image. In terms of quantitative evaluation of image quality, SSIM value of the retrieved SAXGI image is up to 0.9273 and PSNR reaches 29.778 dB, which implicates that SAXGI is capable to obtain high-fidelity images at such few measurements.

The quality of images in different resolution regions reconstructed by the same measurements is intuitively different, and the sparser the image structure, the better the reconstruction quality. The results in Fig. 4 confirms the above conclusion. In Figs. 4(a) and 4(b), the corresponding resolution regions including 15 μm, 10 μm, 7 μm, 5 μm, 4 μm, 3 μm and

2 μm, are marked with different colors. The reconstruction quality of different resolution regions is displayed in Fig. 4(c). The result demonstrates that the image quality evaluation metrics, including PSNR and SSIM, are both improving as the stripe spacing expands in the RC. The SSIM of the 2 μm resolution region reconstructed by SAXGI using 360 measurements is only 0.5593, much lower than the SSIM of 0.9474 for the 15 μm resolution region. Similarly, the PSNR of the 2 μm resolution region is 25.5483, also lower than the PSNR of 30.879 for the 15 μm resolution region. When the stripe spacing exceeds 10 μm, neither peak signal-to-noise ratio and structural similarity rises significantly, which shows that using 360 measurements, the ynthetic aperture x-ray ghost imaging is able to perfectly retrieve the image with the spatial structure larger than 10 μm under the current circumstances of noise and pixel resolution.

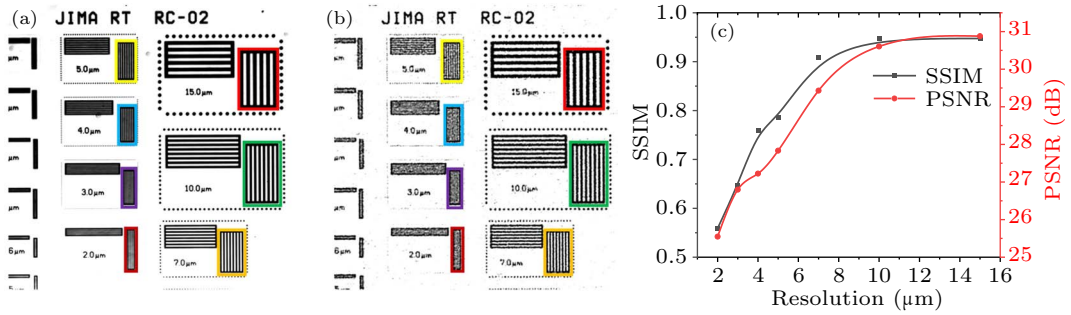


Fig. 4. Quality assessment in different resolution regions. (a) Resolution chart taken by the high-resolution reference detector with the pixel resolution of 0.65 μm. (b) The image reconstructed by SAXGI using 360 measurements at 40×40 binning in object beam. (c) PSNR and SSIM of resolution regions marked with different colors in panels (a) and (b).

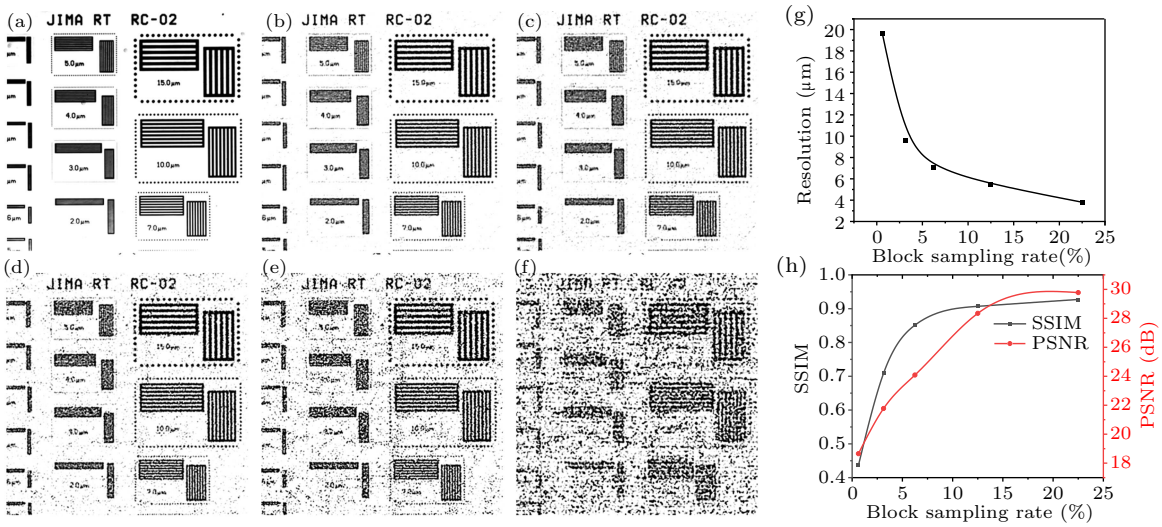


Fig. 5. Quality evaluation and resolution assessment of the resolution chart reconstructed by SAXGI using different measurements. Panel (a) is the image of resolution chart taken by the high-resolution reference detector. Panels (b), (c), (d), (e), and (f) are respectively the images reconstructed by SAXGI using 360, 200, 100, 50, and 10 measurements. Panels (g) and (f) are respectively the resolution assessment and quality evaluation of the reconstructed images using different measurements.

What is more, we also need to discover that the lower limit on the number of measurements for which SAXGI can successfully reconstruct the RC and the resolution SAXGI can achieve at this lower limit. The target image of the resolution chart is shown in Fig. 5(a). As shown in Figs. 5(b)–5(d) are the images reconstructed by SAXGI using 360, 200, 100, 50, and 10 measurements respectively. There is no doubt that the image quality gradually decreases as the measurement number decreases, which agrees well with the result of Fig. 5(h). It has already been mentioned in the previous text that the SSIM of the reconstructed image at 360 measurements is 0.9273 and the corresponding PSNR is 29.778. While the SSIM of the reconstructed image at 10 measurements is only 0.4363 and the PSNR is 18.656, lower than that of the reconstructed image using more measurements. With the measurements increasing to 360 corresponding to the sampling rate of 22.5%, the image quality gradually improves and reaches a limit, revealed by PSNR and SSIM shown in Fig. 5(h). Additionally, according to the criteria of the FRC, the resolution that SAXGI can achieve also deteriorates as the measurement number decreases, as shown in Fig. 5(g). For example, SAXGI can achieve 19.587 μm at 10 measurements while 9.5687 μm at 50 measurements. In fact, through the observation of 7 μm resolution region in the reconstructed image using 50 measurements shown in Fig. 5(e), the stripes are clearly recognizable. It demonstrates that SAXGI can achieve finer resolution than

that FRC gives. The same conclusion can be drawn through identifying the reconstructed image of the 10-μm resolution region using 10 measurements, shown in Fig. 5(f). According to the trend of the curve in Fig. 5(g), the resolution that SAXGI is capable to achieve will reach the resolution limit of about 3 μm, which approaches the limit that the direct radiology can achieve with the pixel size of 0.65 μm. In other words, 360 measurements are enough to obtain the ideal resolution.

3.2. Biological specimen

A fish is adopted to evaluate the potential of SAXGI for imaging a biological specimen with complex structure and relatively low absorption contrast. A small fish (poecilia reticulata) was naturally dried for two weeks and then made into an experimental specimen without destructing its internal structure. Similarly, the same detector was used in reference and object beam in the SAXGI experiments of the fish and the exposure time was 6 s. Given in Fig. 6(a) is the target image with 2000×1000 pixels and effective pixel size of 3.25 μm, captured with the reference detector and exposure time of 3 s, in which microstructures of the fish including skeleton, inconspicuous flesh and fins can be observed distinctly. As shown in Fig. 6(b), the structure of the fish was not revealed by the modulated signals with an effective pixel of 130 μm by a 40×40 binning in the signal beam.

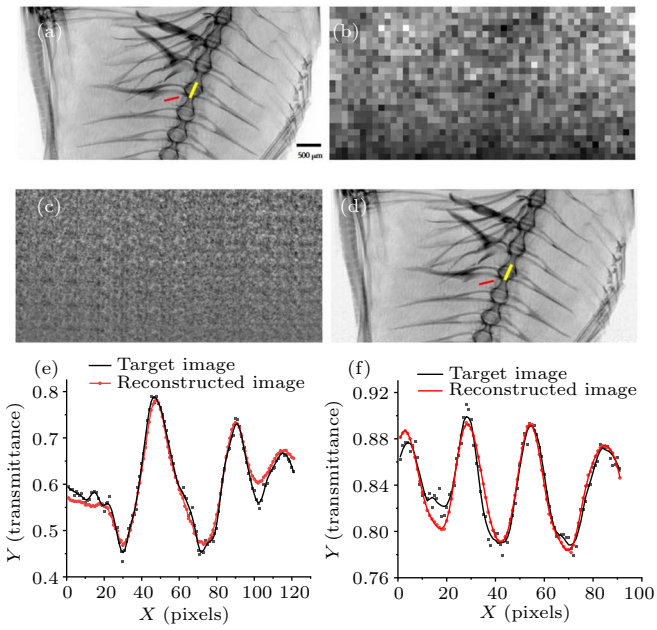


Fig. 6. Experimental results for a dehydrated fish with 770 measurements, where (a) target image taken by high-resolution reference detector with the pixel size of 3.25 μm, (b) signals in object beam with a binning of 40×40, (c) image reconstructed by TXGI, (d) image reconstructed by SAXGI, (e) line profiles of the image area denoted with yellow lines in panels (a) and (d), (f) line profiles of the image area denoted with red lines in panels (a) and (d).

The TXGI was employed to recover the lost information of Fig. 6(b) and the result is shown in Fig. 6(c). Due to measurements used for the TXGI image reconstruction being as low as 770 compared with the tremendous pixel number of the target image, TXGI failed to reveal any useful structure information of the fish. Finally, the proposed SAXGI method is attempted to reconstruct the high-resolution information by correlating the low-resolution signals in the signal beam with the high-resolution speckle patterns in the reference beam. The sampling rate up to 48% was employed to guarantee high-quality reconstruction of the SAXGI image, on the account that biological specimens usually possessed low contrast and high complexity. As shown in Fig. 6(d), the features concerning the microstructure of the fish are revealed clearly in the image reconstructed by SAXGI. To compare the result of SAXGI with the target image, line profiles of grayscale at positions denoted with red and yellow lines in Figs. 6(a) and 6(d) are investigated. The results are shown in Figs. 6(e) and 6(f), in which line profiles of the backbone and the flesh are fairly consistent with that of the target image.

The successful reconstruction with SAXGI using few measurements mainly attributes to the block-by-block strategy. In this experiment, the block size is 40×40 pixels and usually more than 1600 measurements were needed for a conventional reconstruction based on correlation. Instead, only 770 measurements are implemented which infers an obviously insufficient measurements even for a single block. According to Fig. 6(e), features of the backbone are reconstructed with high accuracy relative to the target image. As to the features of flesh, the overall outline of the profile from SAXGI is concordant to that of the target image as shown in Fig. 6(f). However, at locations with lower contrast the detailed microstructures are lost to a certain extent. This means that accuracy of SAXGI for features of low-contrast tissues is interior to that of high contrast tissues, which implicates that more measurements are needed for the accurate reconstruction of samples with complex structure and low contrast.

The SSIM value of the reconstructed fish image by SAXGI is 0.962, which means that the proposed SAXGI method is able to reveal almost all the details of the biological specimen. As a result, the SAXGI is capable to efficiently reproduce a high-quality mega-pixel image of a biological sample with large field of view at few measurements, which also implicates the potential application of SAXGI to biomedical imaging with low radiation dose.

3.3. Estimation of exposure reduction

For a given x-ray source and imaging setup, the radiation exposure of the sample is proportional to the exposure time. To obtain acceptable SNR, for a pixel-array detector the number of photons N_p incident on a binned pixel of the detector is given as following:

$$N_p = k \times \tau_n \times n_1 \times n_2, \tag{1}$$

where k is a constant related to a specific detector, τ_n denotes the exposure time, n_1 and n_2 are the number of pixels used for detector binning during data acquisition and area of the binned pixel is proportional to $n_1 \times n_2$. And then, we have

$$\tau_n = \frac{N_p}{k \times n_1 \times n_2}. \tag{2}$$

The exposure time given in Eq. (2) implicates that the radiation exposure is inversely proportional to the pixel area. In SAXGI, the bucket detector in the signal beam is synthesized by $n_1 \times n_2$ binning over the adjacent pixels of the detector in the reference beam. For an experiment with M measurements, the radiation exposure D_{GI} of the sample during the data acquisition of SAXGI can be expressed as

$$D_{GI} = C \times M \times \frac{N_p}{k \times n_1 \times n_2} = \frac{M}{n_1 \times n_2} \times D_{TR}, \tag{3}$$

where C is a constant related to radiation exposure in a specific experiment, $D_{TR} = C \times N_p/k$ is the radiation exposure for a corresponding traditional radiology on the condition that the detectors before and after binning have the same sensitivity, $M/(n_1 \times n_2)$ is the block sampling rate of SAXGI. According to Eq. (3), if the absorption of the mask is not taken into account, the radiation exposure of ghost imaging is $M/(n_1 \times n_2)$ times of the traditional radiology. This means that in classical XGI with sampling rate set to one, the radiation exposure is the same as that in conventional radiology which is consistent with the results in Ref. [40]. To reduce measurements is the premise for low dose XGI. Limiting the number of measurements and meanwhile remaining a sufficient sampling rate are the practical way to reduce the data acquisition time of XGI and restore images with acceptable SNR. Obviously, SAXGI is the promising solution to implement this strategy.

SAXGI images for the fish restored with different measurements are investigated concerning the radiation exposure. For a fixed 40×40 binning of the detector in the signal beam, the radiation exposure is proportional to the number of measurements. Shown in Fig. 7 are the images restored with a series of measurements of 400, 200, 50 and 10 respectively. Figure 7(a) demonstrates that the SAXGI image reconstructed with measurements of 400 reveals the details of flesh texture and skeleton of the fish. With the measurements reduced, the noise accumulates and the structure information gets lost gradually, as shown in Figs. 7(b)–7(d). Image shown in Fig. 7(d) was reconstructed with 10 measurements, which corresponds to a block sampling rate of $1/160$ in the signal beam of SAXGI. The whole figures of the fish skeleton are still retrieved apparently at such a low sampling rate, which means that SAXGI is able to obtain the skeleton structure of the fish with 0.63% of the radiation exposure in conventional radiology. Therefore, much lower radiation exposure is needed to extract effective information by SAXGI compared to conventional radiology.

To appraise the restored image quality, corresponding values of PSNR and SSIM are also given. The results are shown in Table 1. It is obvious that the radiation exposure decreases with the measurements at an expense of deteriorated image quality. When the number of measurements exceeds 400, no significant enhancement of both PSNR and SSIM can be observed, as shown in Figs. 7(e) and 7(f). In other words, the image reconstructed with similar image quality to that of conventional radiology is achieved at 400 measurements and the corresponding radiation exposure is a quarter of it. This means that SAXGI is able to image a sample with one fourth of radiation exposure in conventional radiology while the image quality is almost the same.

Table 1. Radiation exposure and image quality of SAXGI corresponding to measurements.

Measurements	Radiation exposure*	PSNR	SSIM
770	0.4812	31.62	0.9621
600	0.3750	31.57	0.9616
400	0.2500	31.36	0.9592
200	0.1250	30.77	0.9521
50	0.0313	29.54	0.9349
25	0.0156	29.10	0.9272
16	0.0100	28.93	0.9209
10	0.0063	28.74	0.9179

*With the radiation exposure in conventional radiology set to 1.

With the measurements reduced to 200, the radiation exposure drops to one eighth at an expense of deterioration in image quality while the structure details including the flesh texture and skeleton are still depicted explicitly as shown in Fig. 7(b). After that, the image quality declines evidently with the measurements. When measurements drop to 10, the deterioration of image quality is significant, but the skeleton of the fish is still revealed integrally as shown in Fig. 7(d). Due to the sparse and binary property of the bones, the whole skeleton was successfully reconstructed with compressive sensing based on TV regularization at an extremely low sampling rate. The corresponding radiation exposure is 1/160 of that for conventional radiology, which infers that two orders lower radiation exposure is achievable with SAXGI while the interested structure of the sample is relatively simple, and the associated contrast is fairly high.

Actual radiation exposure at different number of measurements is also evaluated quantitatively according to Eq. (3) and the related experimental parameters. The flux density of x-ray beam at 15 keV of BL09B at SSRF is 7.5×10^8 photons/s/mm^2. The image size in the experiments is 2000×1000 pixels with size of 3.25 mm and

6.5 mm×3.25 mm. Thus, the total flux incident on the sample is 7.9×10^9 photons/s considering the 50% absorption of the sandpaper. According to the flat image without sample and the sample image, the averaged absorption rate of the fish is 0.172. The exposure time for the target image is 3 s and the radiation exposure of the fish is 4076 photons/pixel, which meets the requirements to obtain high contrast imaging of biomedical samples in conventional radiology. The SAXGI is anticipated to reduce that radiation exposure tremendously. Taking into account the 40×40 binning of the detector, the effective exposure time for each frame in the signal beam is 3.75 ms. Accordingly, the average radiation exposure is 2.55 photons/pixel in each measurement. Furthermore, two orders higher efficiency compared to the scintillator-based detector used in our experiments, can be achieved according to the published results,[21] if a direct recording x-ray detector is employed in the signal beam.

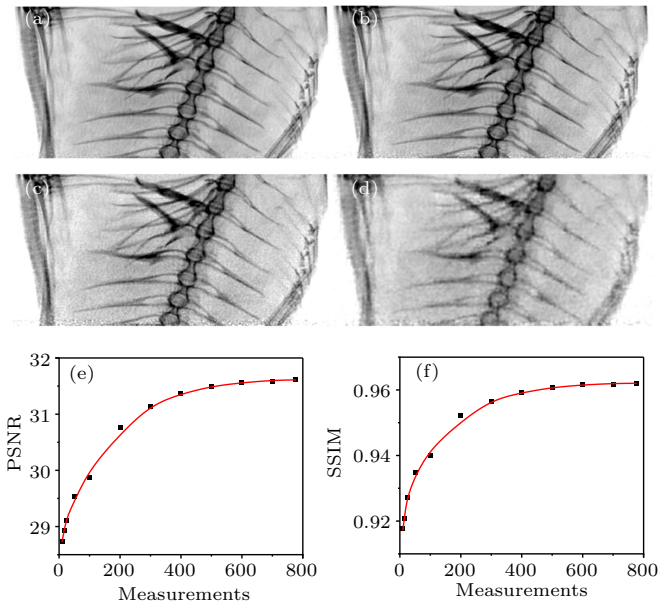


Fig. 7. SAXGI images for a fish reconstructed with measurements of (a) 400, (b) 200, (c) 50, and (d) 10 at a 40×40 binning of the detector in the signal beam. Panels (e) and (f) depict that PSNR and SSIM vary with the measurements, respectively.

The number of measurements is the key issue to control radiation exposure in XGI. Based on the strategy in SAXGI, the number of measurements for a mega-pixel XGI can be reduced to a quite low level. According to the experimental results, 400 measurements is able to restore images of similar quality to conventional radiology and the correspondent radiation exposure is 1019 photons/pixel which is one-fourth of the conventional radiology. The lower limit of measurements in SAXGI is 10, which is sufficient to discern the skeleton of the fish and the overall radiation exposure is reduced to 25.5 photons/pixel which is far less than that of conventional radiology. Furthermore, by combining SAXGI with a direct recording x-ray detector in the signal beam, the expected overall radiation exposure for SAXGI is 10.19 photons/pixel at 400 measurements and 0.255 photons/pixel at 10 measurements respectively. In fact, this is also the advantage of XGI as a nonlocal imaging method, in which detectors of different efficiencies can be selected to record the images in reference and signal beam respectively. Combining the synthetic aperture strategy of SAXGI with the nonlocal property of XGI, x-ray ghost imaging with mega-pixel and low radiation exposure is promising.

4. Discussion and conclusion

Synthetic aperture x-ray ghost imaging (SAXGI) has great potential in low dose radiology and high resolution. Firstly, a resolution chart, a typical binary object with low contrast and relatively simple structure is employed to evaluate the spatial resolution of SAXGI. The image of 1960×1960 pixels was reconstructed with a 40×40 binning in the object beam at 360 measurements. According to visibility of the resolution chart, SAXGI can achieve a spatial resolution of 4 μm, which is close to the resolution limit of conventional radiography with the pixel resolution of 0.65 μm. with measurements reduced to 10, the resolution of 10-μm SAXGI can obtain exceeds the 26-μm pixel resolution of the signal detector. Moreover, A dehydrated fish was adopted to test the ability of SAXGI for low-contrast and complex samples. The microstructures of the fish including the skeleton, flesh and fins exhibited in 2000×1000 pixels were definitely reconstructed by SAXGI with a 40×40 binning in the object beam at 770 measurements. Estimation of radiation exposure compared with conventional radiology was also carried out. One fourth of the radiation exposure in conventional radiology was achieved by SAXGI at 400 measurements while the image quality remains almost the same. When measurements drop to 10, which corresponds to 1/160 of radiation exposure in conventional radiology, skeleton of the fish was still revealed integrally by SAXGI. Therefore, we can conclude that the proposed SAXGI enables high-fidelity imaging at radiation exposures at least two orders of magnitude lower than conventional x-ray imaging. Accordingly, these results demonstrate that SAXGI is able to restore a megapixel image with high fidelity and few measurements.

The strategy of SAXGI to reconstruct the images block by block reduces tremendously the requirements on the number of measurements. Combined with TV regularization in compressive sensing, the number of the measurements is further reduced significantly and the robustness of SAXGI against optical background noises is also improved. Much fewer measurements of the proposed method represents not only low ra-

diation exposure but also high efficiency for data acquisition. Results of this paper implicate that SAXGI provides a practical approach for the implementation of low-dose x-ray ghost imaging for non-destructive imaging of a variety of samples, especially biomedical specimens.

Acknowledgement

Project supported by the National Key Research and Development Program of China (Grant Nos. 2022YFA1603601, 2021YFF0601203, and 2021YFA1600703).

References

[1] Tao F, Wang J, Du G, Su B, Zhang L, Hou C, Deng B and Xiao T 2023 *Journal of Synchrotron Radiation* **30** 815
[2] Voegeli W, Kajiwara K, Kudo H, Shirasawa T, Liang X and Yashiro W 2020 *Optica* **7** 514
[3] Davis T J, Gao D, Gureyev T E, Stevenson A W and Wilkins S W 1995 *Nature* **373** 595
[4] Chen R C, Rigon L and Longo R 2013 *Opt. Express* **21** 7384
[5] Liu Z D, Zhong J Y, Yuan X H, Zhang Y P, Yao J W, Ma Z L, Xu X Y, Xue Y H, Zhang Z, Yuan D W, Zhang M R, Li B J, Gu H C, Dai Y, Zhang C L, Dong Y F, Zhou P, Ma X J, Ma Y F, Bai X J, Liu G Y, Tian J S, Zhao G and Zhang J 2023 *Chin. Phys. B* **32** 110702
[6] Wang Z L, Chen Z H, Gu Y, Chen H and Ge X 2023 *Chin. Phys. B* **32** 038704
[7] Sun Z, Tuitje F and Spielmann C 2021 *Journal of Microscopy* **284** 3
[8] Sefi O, Ben Yehuda A, Klein Y, Sobol Z, Bloch S, Schwartz H, Cohen E and Shwartz S 2024 *Opt. Express* **32** 37001
[9] Zhang D J, Tang Q, Wu T F, Qiu H C, Xu D Q, Li H G, Wang H B, Xiong J and Wang K 2014 *Appl. Phys. Lett.* **104** 121113
[10] Chen X H, Agafonov I N, Luo K H, Liu Q, Xian R, Chekhova M V and Wu L A 2010 *Opt. Lett.* **35** 1166
[11] Chen X H, Liu Q, Luo K H and Wu L A 2009 *Opt. Lett.* **34** 695
[12] Zhang M, Wei Q, Shen X, Liu Y, Liu H, Cheng J and Han S 2007 *Phys. Rev. A* **75** 021803
[13] Li S, Cropp F, Kabra K, Lane T J, Wetzstein G, Musumeci P and Ratner D 2018 *Phys. Rev. Lett.* **121** 114801
[14] Cao M, Yang X, Wang J, Qiu S, Wei D, Gao H and Li F 2016 *Opt. Lett.* **41** 5349
[15] Kingston A M, Myers G R, Pelliccia D, Salvemini F, Bevitt J J, Garbe U and Paganin D M 2020 *Phys. Rev. A* **101** 053844
[16] Pelliccia D, Olbinado M P, Rack A, Kingston A M, Myers G R and Paganin D M 2018 *IUCrJ* **5** 428
[17] Zhao C Z, Zhang H P, Tang J, Zhao N X, Li Z L and Xiao T Q 2024 *Journal of Synchrotron Radiation* **31** 1525
[18] Kingston A M, Pelliccia D, Rack A, Olbinado M P, Cheng Y, Myers G R and Paganin D M 2018 *Optica* **5** 1516
[19] Klein Y, Sefi O, Schwartz H and Shwartz S 2022 *Optica* **9** 63
[20] Olbinado M P, Paganin D M, Cheng Y and Rack A 2021 *Optica* **8** 1538
[21] Zhang A X, He Y H, Wu L A, Chen L M and Wang B B 2018 *Optica* **5** 374
[22] Klein Y, Schori A, Dolbnya I P, Sawhney K and Shwartz S 2019 *Opt. Express* **27** 3284
[23] Schori A and Shwartz S 2017 *Opt. Express* **25** 14822
[24] Manni M, Ben-Yehuda A, Klein Y, Lukic B, Kingston A, Rack A, Shwartz S and Viganò N 2023 *Opt. Lett.* **48** 6271
[25] Ceddia D and Paganin D M 2018 *Phys. Rev. A* **97** 062119
[26] Pelliccia D, Rack A, Scheel M, Cantelli V and Paganin D M 2016 *Phys. Rev. Lett.* **117** 113902
[27] Yu H, Lu R, Han S, Xie H, Du G, Xiao T and Zhu D 2016 *Phys. Rev. Lett.* **117** 113901
[28] Wang F, Hua W, Zhao C, Zhang H, Yang S, Li X, Deng B, Xie H and Xiao T 2024 *Phys. Rev. Res.* **6** 043293
[29] Zhang H, Li K, Wang F, Yu H, Zhao C, Du G, Li Z, Deng B, Xie H L, Han S and Xiao T J C O L 2022
[30] Zhang H, Li K, Zhao C, Tang J and Xiao T 2022 *Chin. Phys. B* **31** 064202
[31] Zhang H P, Zhao C Z, Ju X L, Tang J and Xiao T Q 2022 *Acta Phys. Sin.* **71** 074201 (in Chinese)
[32] Ben-Yehuda A, Sefi O, Klein Y, Schwartz H, Cohen E, Shukrun R H and Shwartz S 2024 *Communications Engineering* **3** 39
[33] Zhao C Z, Si S Y, Zhang H P, Xue L, Li Z L and Xiao T Q 2024 *Chin. Phys. B* **33** 014102
[34] Katayama T, Inubushi Y, Obara Y, Sato T, Togashi T, Tono K, Hatsui T, Kameshima T, Bhattacharya A, Ogi Y, Kurahashi N, Misawa K, Suzuki T and Yabashi M 2013 *Appl. Phys. Lett.* **103** 131105
[35] Klein Y, Strizhevsky E, Capotondi F, De Angelis D, Giannessi L, Pancaldi M, Pedersoli E, Prince K C, Sefi O, Kim Y Y, Vartanyants I A and Shwartz S 2022 *Frontiers in Optics + Laser Science* 2022 *(FIO, LS)*, 2022/10/17, Rochester, New York, p. LW7F.4
[36] Sefi O, Klein Y, Strizhevsky E, Dolbnya I P and Shwartz S 2020 *Opt. Express* **28** 24568
[37] Aminzadeh A, Roberts L, Young B, Chiang C I, Svalbe I D, Paganin D M and Kingston A M 2023 *Opt. Express* **31** 24328
[38] Huang Y, L?sel P D, Paganin D M and Kingston A M 2024 *Phys. Rev. A* **110** 063512
[39] Zhang H, Du K, Zhao C, Tang J, Si S, Jia W, Xue L and Li Z 2023 *Sci. Rep.* **13** 22702
[40] Kingston A M, Fullagar W K, Myers G R, Adams D, Pelliccia D and Paganin D M 2021 *Phys. Rev. A* **103** 033503
[41] Zhao C Z, Si S Y, Zhang H P, Xue L, Li Z L and Xiao T Q 2022 *Acta Phys. Sin.* **71** 046101 (in Chinese)
[42] Yu X, Stantchev R I, Yang F and Pickwell-MacPherson E 2020 *Sci. Rep.* **10** 9338
[43] Sun M J, Meng L T, Edgar M P, Padgett M J and Radwell N 2017 *Sci. Rep.* **7** 3464
[44] Katz O, Bromberg Y and Silberberg Y 2009 *Appl. Phys. Lett.* **95** 131110
[45] Higham C F, Murray-Smith R, Padgett M J and Edgar M P 2018 *Sci. Rep.* **8** 2369
[46] He Y, Wang G, Dong G, Zhu S, Chen H, Zhang A and Xu Z 2018 *Sci. Rep.* **8** 6469